RESEARCH ARTICLE

Wireless Insights Into Cognitive Wellness: A Paradigm Shift in Alzheimer's Detection Through Ultrathin Wearable Antennas

FATMA TAHER [1], (Senior Member, IEEE), **MOATH ALATHBAH** [2], **M. ABDEL-ALEIM M.** [3,4], **THAMER ALGHAMDI** [5], **MOHAMED FATHY ABO SREE** [6], AND **SARA YEHIA ABDEL FATAH** [7,8]

[1] College of Technological Innovation, Zayed University, Dubai, United Arab Emirates
[2] Department of Electrical Engineering, College of Engineering, King Saud University, Riyadh 11451, Saudi Arabia
[3] Department of Electronics and Communications Engineering, Faculty of Engineering, Ahram Canadian University, Cairo 12451, Egypt
[4] Department of Communication and Electronics, Arab Academy for Science, Technology & Maritime Transport, Cairo 11799, Egypt
[5] Wolfson Centre for Magnetics, School of Engineering, Cardiff University, CF10 3AT Cardiff, U.K.
[6] Department of Electronics and Communications Engineering, Arab Academy for Science, Technology & Maritime Transport, Cairo 451913, Egypt
[7] Department of Mechatronics Engineering and Automation, Faculty of Engineering, Egyptian Chinese University, Cairo 19346, Egypt
[8] Higher Institute of Engineering and Technology, EL-Tagmoe EL-Khames, New Cairo City 11765, Egypt

Corresponding author: Thamer Alghamdi (alghamdit1@cardiff.ac.uk)

ABSTRACT The Proposed algorithm, designed to simulate an Alzheimer's disease (AD) brain model across different stages, presents an invaluable opportunity for further research and in-depth study of the effects of AD. Currently, there is a notable absence of a comprehensive simulated model for the AD brain that allows the exploration of all AD biomarkers within a simulation tool. This represents a crucial advancement in the field, enabling researchers to thoroughly investigate and understand the diverse biomarkers associated with AD without resorting to highly expensive and ionizing radiation techniques. The algorithm's capability to emulate various stages of AD in a simulated environment is an essential step toward assessing its applicability for AD patients, providing a cost-effective and safer alternative for research and study in comparison to existing methodologies and delves into the development and evolution of a patch antenna designed for the identification of distinct stages in Alzheimer's disease (AD) detection. The antenna, equipped with ultra-wideband (UWB) capabilities, consists of a slotted circular disc antenna patch and a partial ground. The placement of rectangular slots in the ground structure aims to enhance radiation directivity, gain, and efficiency. The primary objective is to optimize the antenna's efficacy by strategically integrating a slotted circular disc and arranging slots in the ground structure. The research aims to provide an effective solution for non-invasive tracking of Alzheimer's disease progression. The antenna, with dimensions of $50 \times 35 \times 0.1$ mm^3, is fabricated using a flexible laminate substrate (Ultra-lam 3850). The prototype demonstrates a remarkable bandwidth of 8.55 GHz (2.02–10.57 GHz) and exhibits nearly directional radiation characteristics. The study employs 3D CST 2019 simulator software for analysis, followed by physical fabrication and measurement of the antenna. Evaluation involves both a single antenna and a four-antenna array element around a 3D realistic-shaped Hugo head model and a six-layer brain phantom simulating various AD stages. The reported peak gain reaches 2.36 dBi and 3.1 dBi at 2.4 GHz and 7.48 GHz, respectively, with consistently high radiation efficiency (92.5% and 90.5% at 2.4 GHz and 7.48 GHz).

The associate editor coordinating the review of this manuscript and approving it for publication was Valentine Novosad.

In practical application, the antenna demonstrates satisfactory field penetration into human head tissues while adhering to safety standards. Specific Absorption Rate (SAR) values of 0.734 W/kg and 0.00238 W/kg at 2.4 GHz and 7.48 GHz, respectively, ensure compliance with safety regulations. The research concludes that the proposed antenna, supported by statistical and measured data, presents a promising non-invasive method for effectively tracking the progression of Alzheimer's disease.

INDEX TERMS An ultra-wideband patch antenna, Alzheimer's disease, medical diagnosis, six-layer brain phantom, radio frequency.

I. INTRODUCTION

Alzheimer's disease (AD) is the predominant form of neurodegenerative illness, ranking as the sixth leading cause of death in the United States [1], [2]. According to data from the Alzheimer's Association, AD incurs the highest healthcare costs in the U.S., exceeding expenses related to cancer and heart disease, with care costs estimated at around $290 billion in 2019 [3]. It stands as the leading cause of death among women and the second leading cause among men in the U.K. [4]. The Alzheimer's Society in the U.K. reports a population of over 520,000 individuals with AD out of the 850,000 affected by dementia, projecting an increase to 1 million by 2025 [5]. AD initiates pathological changes in the brain, characterized by progressive atrophy, particularly in the hippocampus, and an enlargement of the lateral ventricles [6]. Histologically, the primary modifications in AD involve the gradual accumulation of beta-amyloid plaques and tau neurofibrillary tangles [7].

The block diagram presented in Figure 1 delineates the categorization of biomedical antennas into two main groups: communication antennas and detection antennas. Detection antennas [8] are intricately crafted for sensing and imaging applications within biomedical contexts, tasked with detecting and capturing signals or electromagnetic waves generated by the body or medical devices. These antennas play a pivotal role in various diagnostic techniques, including magnetic resonance imaging (MRI), computed tomography (CT), ultrasound, and microwave imaging. Their design is meticulously optimized to receive and convert signals into measurable data, forming a crucial step in the subsequent analysis for disease detection, monitoring, or localization.

Figure 2 likely outlines specific challenges associated with biomedical antennas 9, and addressing these challenges demands a comprehensive, interdisciplinary approach. This approach encompasses expertise in antenna design, electromagnetic simulation, signal processing, and medical imaging. Collaboration among professionals from diverse fields, such as engineers, physicists, radiologists, and medical practitioners, is paramount in the development of effective breast cancer detection systems. This collaborative effort holds the potential to make a positive impact on healthcare by advancing the capabilities of biomedical antennas in disease detection and monitoring.

Microwave sensing and imaging systems have gained considerable attention due to their attributes of being cost-effective, flexible, compact, non-invasive, and non-ionizing.

Operating within the non-ionizing frequency spectrum [10], microwave technology utilizes electromagnetic waves capable of penetrating tissues, rendering it suitable for diagnostic purposes. Recent innovations in microwave sensing techniques have been deployed to identify various medical conditions, including tumors, brain strokes, Alzheimer's, and breast cancer. There is a specific emphasis on achieving high temporal resolution for functional neuroimaging. These methodologies exploit variations in dielectric permittivity and electrical conductivity between healthy and unhealthy body regions, employing antenna arrays to transmit and receive signals for accurate diagnosis and disease analysis. The incorporation of Ultra-wideband (UWB) technology further improves the resolution and precision of microwave imaging systems. Ongoing research in the field is dedicated to advancing the detection of neurodegenerative conditions using microwave sensors. It's important to highlight that there is a lack of research on the detection of Huntington's disease and multiple sclerosis using microwave technology. However, there have been limited studies on the application of microwave technology in detecting Parkinson's and Alzheimer's diseases, which will be explored in the following two subsections. The implementation of the microwave helmet brain scanner imaging systems is straightforward, following standard procedures outlined in various RF engineering literatures for the design of microstrip/patch array (transmit/receive pair) antennas. The prototype's antenna characteristics showcase its potential for wide-band application, greatly facilitating imaging processing. These systems are comprised of RF transmitter/receiver modules and accessories interfacing with a high-speed digital image processor. The low-cost microwave brain scanner produces visual images displaying the activities of Parkinson's Disease (PD) patients. Employing 3D holography-based imaging algorithms, as found in general literature [11]. A notable development is a wearable hat featuring six ultra-wideband monopole bidirectional antenna elements arranged symmetrically, designed to detect brain atrophy by capturing alterations in brain volume and cerebrospinal fluid through reflection coefficient measurements [12]. Another pioneering design utilizes a six-element stepped monopole wideband antenna for detecting beta-amyloid plaques and tau tangles associated with Alzheimer's disease [13]. This study expands its scope to explore the dielectric properties of affected brain tissues, offering valuable insights through measurements of relative permittivity and conductivity. The findings,
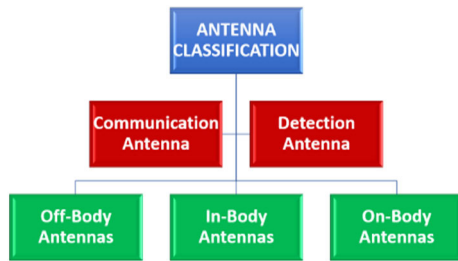
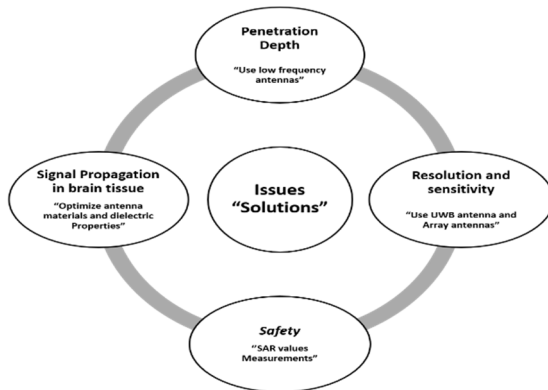**FIGURE 1.** Categorization of antennas in the biomedical field.

FIGURE 2. Challenges and possible solution for Brain diagnosis antenna design.

emphasizing discernible changes in conductivity and dielectric permittivity due to the presence of plaques and tangles, not only enhance Alzheimer's detection but also present potential applications for identifying various other neuropathologies [14].

In the past decade, the predominant focus of research has been on the identification and imaging of neurodegenerative diseases, notably Alzheimer's disease. Earlier investigations utilized computed tomography (CT) and magnetic resonance imaging (MRI) to exclude other potential causes of dementia. A more recent tool, structural MRI, has been developed to assess atrophy and changes in tissue characteristics. MRI, renowned for its widespread availability, has been strongly recommended in dementia diagnosis within European and U.S. medical practices [14]. However, the associated high costs may present a barrier for some patients, and accessibility might be constrained in certain countries. Moreover, individuals with severe cases of Alzheimer's disease may face challenges in tolerating both MRI and CT scan procedures. The authors have previously explored RF sensing for the detection of brain atrophy and lateral ventricle enlargement [14], [15]. These devices offer advantages such as cost-effectiveness, a low-profile design, and non-ionizing properties. Nevertheless, the transition to clinical application is still in its early stages. Several studies have also delved into the dielectric properties of brain tumors and strokes, but, to the best of the authors' knowledge, no studies have reported on measuring dielectric properties for a brain affected by

Alzheimer's disease (AD). More recently, researchers have investigated the use of implantable antennas to identify the presence of beta-amyloid proteins in cerebrospinal fluid (CSF) from canines [16]. Nonetheless, the use of implantable antennas is invasive and may not be convenient for patients.

The contributions of this paper are multi-faceted:

- **Innovative AD Brain Model Algorithm:** The introduction of a novel algorithm for simulating an Alzheimer's disease (AD) brain model across various stages stands out as a significant contribution. This algorithm addresses a crucial gap in the field by providing a comprehensive simulated model that allows for the exploration of all AD biomarkers within a simulation tool.
- **Advancement in AD Detection Patch Antenna:** The paper introduces a pioneering patch antenna specifically designed for Alzheimer's disease detection. Equipped with ultra-wideband (UWB) capabilities, this antenna incorporates a slotted circular disc and a strategically designed partial ground, enhancing radiation directivity, gain, and efficiency. This innovation presents a promising non-invasive solution for tracking the progression of AD.
- **Optimized Antenna Fabrication and Evaluation:** The study showcases meticulous attention to detail in the fabrication of the patch antenna. With dimensions of $50 \times 35 \times 0.1$ mm^3 and utilizing a flexible laminate substrate (Ultra-lam 3850), the antenna's physical characteristics are optimized. The comprehensive evaluation, encompassing 3D simulation analysis and physical measurements, underscores the antenna's performance in both single and arrayed configurations.
- **Detailed Assessment of Antenna Performance:** The paper provides detailed insights into the performance of the patch antenna, reporting peak gains of 2.36 dBi and 3.1 dBi at 2.4 GHz and 7.48 GHz, respectively. Consistently high radiation efficiency (92.5% and 90.5% at 2.4 GHz and 7.48 GHz) showcases the antenna's efficacy. Practical application involves field penetration into human head tissues while maintaining compliance with safety standards, as indicated by Specific Absorption Rate (SAR) values.
- **Non-Invasive AD Tracking Methodology:** The overarching contribution of this paper lies in offering a non-invasive methodology for effectively tracking the progression of Alzheimer's disease. Supported by statistical and measured data, the proposed antenna and algorithm provide a promising alternative to existing methodologies that often involve high costs and ionizing radiation. This paper opens avenues for further research and study in the critical area of Alzheimer's disease detection and monitoring.

This paper introduces an innovative application of a cost-effective and non-intrusive wearable device designed to track the progression of brain atrophy, lateral ventricle
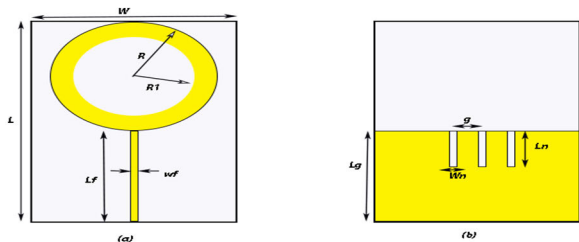
FIGURE 3. Illustration of the envisioned prototype through a geometric model, including (a) a front-side perspective (b) a rear-side perspective.

TABLE 1. All parameters of the proposed prototype.

Parameters	Size (mm)	Parameters	Size (mm)
L	50	R1	10
W	35	Lg	16
wf	0.25	wn	0.25
lf	16	Ln	4
R	17	g	2

enlargement, and detect changes in the dielectric properties of both gray and white matter in individuals with Alzheimer's disease. The document initiates with a thorough examination of the antenna's geometry and design methodology in Section II, followed by the presentation of the design approach in Section III. Section V is dedicated to the analysis of the antenna's performance with human head phantoms, including the Hugo model and six-layer head tissues. In the subsequent phase of this investigation, the employed antenna was utilized to identify brain atrophy, vertical enlargement, and alterations in the dielectric characteristics of gray, white matter, and cerebrospinal fluid (CSF) associated with Alzheimer's disease. Section VI incorporates the modelling of AD using six-layer brain tissues in various stages. The evaluation involved a six-layer brain phantom and the Hugo model, employing both a single antenna and a 4-element array antenna, along with assessing the Specific Absorption Rate (SAR) around the brain. The study is then compared with other relevant works in the field, as detailed in Section VII.

II. GEOMETRY EXAMINATION FOR THE PROPOSED ANTENNA

This section elucidates the design process of the proposed Ultra-Wideband (UWB) antenna, which is compact and flexible, built around a circular disc monopole. Notable for its lightweight and low-profile characteristics, the antenna facilitates seamless integration with the substrate. Figures 3 (a) and (b) illustrate the design and implementation of the antenna on ULTRALAM 3850 substrate, with a relative permittivity (εr) of 2.9. The metallic (Copper) patch of the antenna has a thickness of $35\mu m$, while the substrate's height is 0.1016 mm. The Ultralam 3850 laminate features a loss tangent (tan δ) of 0.0025. Material parameters for the specified substrate are obtained from the manufacturer Rogers Corporation's datasheet at 10 GHz [17]. To meet the requirements of high-frequency applications, the CST MW studio conducts comprehensive material characterization for both the dielectric constant and the loss tangent.

The choice of the Ultralam 3850 flexible laminate is driven by its exceptional high-frequency characteristics and its resilience to changes in frequency and temperature. This thin material provides the required flexibility for bending, making it well-suited for applications demanding adaptabil-

ity, such as employing the antenna as a textile antenna. The substrate dimensions for the antenna installation are 50 × 35 mm². The circular disc design of the antenna patch has a radius of 17 mm, and a 50-ohm feed line is utilized for patch excitation. All parameters of the proposed prototype are outlined in Table 1. Deliberate perturbations are introduced to both the patch and ground plane as a strategic approach to expand the antenna's bandwidth and achieve resonance at 2.4 GHz. This involves introducing a 20 mm diameter circular slot at the center of the circular patch. The antenna features a partial ground plane, extending over a length of 16 mm. Additionally, narrow rectangular slits, each measuring 4 × 0.25 mm² with a spacing of 2 mm, are incorporated into the ground plane to effectively enhance the overall bandwidth of the antenna, in line with recommendations found in relevant literature [18], [19].

In the realm of a circular disc monopole antenna, the dimension of the disc's diameter (D) carries substantial significance in determining the fundamental mode or the first resonance frequency. It's important to note that at this frequency, the diameter D closely aligns with the corresponding quarter wavelength [20]. For a given disc radius (R) and wavelength (λ) at the fundamental mode, the mathematical relationship can be articulated as follows:

$$D = 2R \approx \frac{\lambda}{4} \qquad \text{[20]} \qquad (1)$$

In the realm of relative permittivity (εr) and the speed of light (C = 3 × 10^8 m/s), the wavelength corresponding to a specified frequency (f) can be computed using the subsequent equation:

$$D = \frac{C}{f\sqrt{\varepsilon r}} \qquad \text{[20]} \qquad (2)$$

In light of the Ultralam 3850 substrate's relative permittivity (εr = 2.9), the computed wavelength (λ) at the fundamental frequency (2.4 GHz) is 293 mm. Importantly, with a circular disc radius (R) of 36.7 mm, the disc's diameter (D) is established at 73.4 mm. However, in the scenario of the slotted circular disc configuration, featuring a circular slot with a radius of 10 mm, a more compact circular disc with a radius of 17 mm is achieved at the 2.4 GHz frequency.

III. DESIGN METHODOLOGY

Figure 4 depicts various adjustments in conjunction with the final configuration of the proposed antenna. This encompasses the influence of standard patch design, including
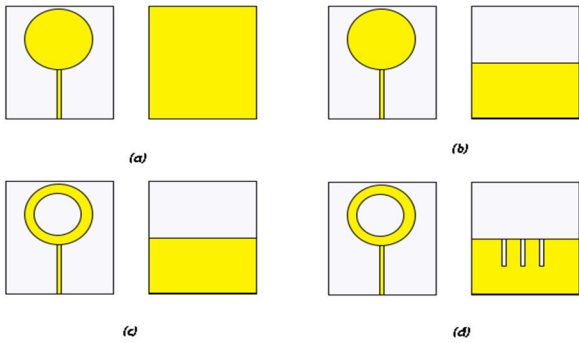
FIGURE 4. Deferent types of layout design of the antenna: (a) Normal patch antenna design with the full ground (b) Normal patch antenna design with partial ground (c) with circular -shaped slot from patch design (d) With a rectangular-shaped slot design.
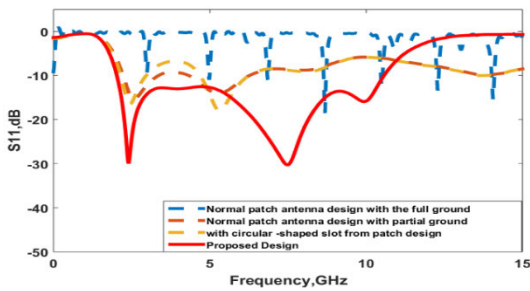

FIGURE 5. Impact of various configurations of the envisioned prototype on simulated S11: (a) with the full ground (b) with partial ground (c) with circular -shaped slot from patch design (d) With a rectangular-shaped slot design.

full ground, partial ground, bottom slotted partial ground, and slotted patch. Initially, circular and rectangular slots are carved out from both the radiating patch and the partial ground, following the dimensions specified in Table 1. Subsequently, a comprehensive analysis of all antenna parameters is executed. In the end, the diverse modified structures yield satisfactory results, demonstrating the intended characteristics of the wideband antenna for Alzheimer's disease (AD) brain diagnosis.

Figure 5a illustrates the reflection characteristics of the standard patch design, incorporating a complete ground plane as depicted in Figure 5a. This particular configuration demonstrates an exceptionally low reflection coefficient, exceeding the −10 dB threshold. As a result, there is no emergence of any frequency band below this specified threshold. Conversely, the standard patch design with a partial ground plane (Figure 5b) produces two distinct frequency bands. The first spans from 2.22 GHz to 3.66 GHz, with a resonance peaking at approximately −15 dB at 2.58 GHz. The second band extends from 4.31 GHz to 6.25 GHz, featuring a resonance frequency of approximately −14 dB at 5.26 GHz. Given that the antenna achieves resonance frequencies below −10 dB due to the partial ground, we opt to proceed with the partial ground plane for further design iterations, incorporating various modifications to the ground structure. Additionally,
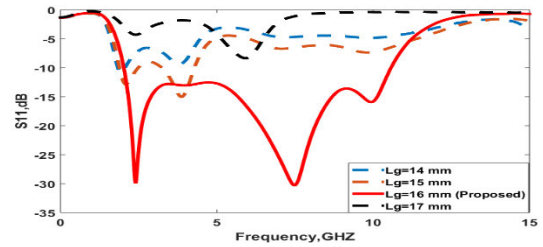

FIGURE 6. The impact of the antenna's reflection coefficient across various ground plane lengths (Lg).

the introduction of a circular slot into the patch (Figure 5c) yields two operational bands with respective resonance frequencies. The first band spans from 2.15 GHz to 2.95 GHz, achieving a resonance frequency near −16 dB. The second band covers 4.70 GHz to 6.27 GHz, with a resonance frequency of approximately −18 dB. Finally, in Figure 5d, the reflection coefficient curve extends from −30 dB at 2.4 GHz and 7.43 GHz within the frequency range of 2.02 GHz to 10.57 GHz. Figure 6 portrays the influence of the ground length 'Lg' on achieving an optimal frequency response. While maintaining consistency with other parameters, setting the ground length to Lg = 17 mm results in the S11 curve surpassing −5 dB, eliminating any frequency band below −10 dB. Conversely, within the Lg range of 14 mm to 15 mm, the S11 curve drops below −10 dB for a single operating frequency at 1.91 GHz and two operating frequencies at 2 GHz and 3.88 GHz, respectively, albeit with insufficient bandwidth. The proposed ground length of Lg = 16 mm attains an ultrawideband performance at 2.4 GHz.

The effective adjustment of the separation parameter 'g' between rectangular slots in the ground plane is pivotal for achieving an expanded bandwidth, as outlined in Figure 7. The narrowest bandwidth, observed at 2.5 GHz, occurs when 'g' is set to 1 mm. Subsequently, an increase in 'g' to 3 mm results in a bandwidth expansion to 6.3 GHz. A marginal bandwidth increase is observed for 'g' set at 2.5 mm, followed by a more substantial increase at 1.5 mm, yielding an 8.2 GHz bandwidth. The peak bandwidth of 8.8 GHz is achieved with 'g' set at 2 mm. The circular slot within the circular disc is instrumental in achieving an operating frequency within the ISM band, particularly at 2.4 GHz. Varying the radius of this slot produces different operating frequencies. For instance, a radius of r1 = 8 mm yields an operating frequency of 2.47 GHz. As the radius increases to 9 mm, the operating frequency becomes 2.44 GHz, and at r1 = 11 mm, the frequency is 2.3 GHz. The optimal radius of r1 = 10 mm achieves the target frequency of 2.4 GHz, as depicted in Figure 8, playing a pivotal role in maintaining a compact antenna dimension. When the 'wn' parameter is varied across 0.1 mm, 0.15 mm, and 0.2 mm, a notably narrow bandwidth of approximately 1.2 GHz is observed. Minimal changes in 'wn' between these values result in a negligible bandwidth shift of around 0.1 GHz. However, setting 'wn' to 0.25 mm yields a significantly broader bandwidth of 8.8 GHz,
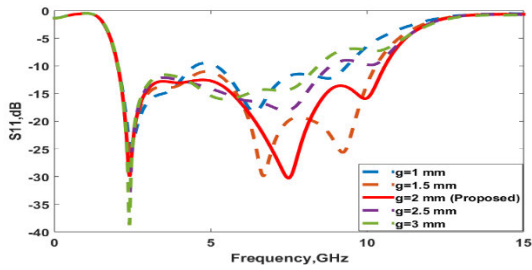
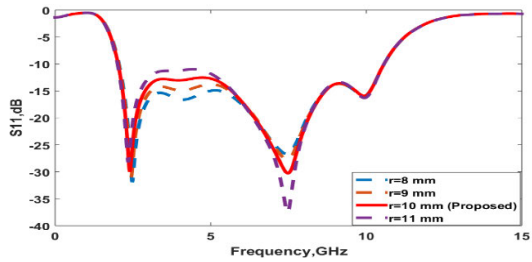**FIGURE 7.** The impact of the antenna's reflection coefficient across various rectangular slits spaces (g).

FIGURE 8. The impact of the antenna's reflection coefficient across various Patch circular slot radiuses (r).
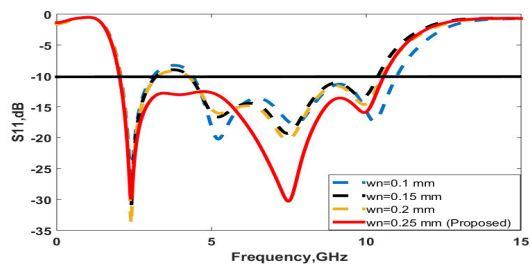

FIGURE 9. The impact of the antenna's reflection coefficient across various ground rectangle slots widths (wn).

FIGURE 10. The impact of the antenna's reflection coefficient across various ground rectangle slots lengths (ln).

FIGURE 11. The impact of the antenna's reflection coefficient across various rectangular slots into ground Plane.

FIGURE 12. Surface current distribution of designed antenna: (a) at 2.4 GHz (b) at 7.48 GHz.

as illustrated in Figure 9. As demonstrated in Figure 10, the 'ln' parameter mimics the behavior of the 'wn' parameter. Varying 'ln' at values of 1 mm, 2 mm, and 3 mm results in a narrower bandwidth of 1.1 GHz, with a minor 0.1 GHz distinction in bandwidth between these values. The maximum bandwidth is achieved at 'ln' = 4 mm. An innovative strategy for enhancing bandwidth involves integrating multiple rectangular slots into the ground plane. Through a specific spacing methodology, this approach yields higher bandwidth, as depicted in Figure 11. For a single slot, the bandwidth is 1.1 GHz. Introducing two slots nearly triples the bandwidth to around 3 GHz, and the addition of three slots results in a substantial bandwidth of 8.8 GHz, accompanied by a commendable efficiency exceeding 92.5% at 2.4 GHz.

IV. ANALYSIS OF THE ANTENNA'S PERFORMANCE
The assessment of the performance of the proposed prototype was carried out using the 3D CST Microwave Studio 2019 software, encompassing measurements for critical parameters such as the reflection coefficient (S11), gain,
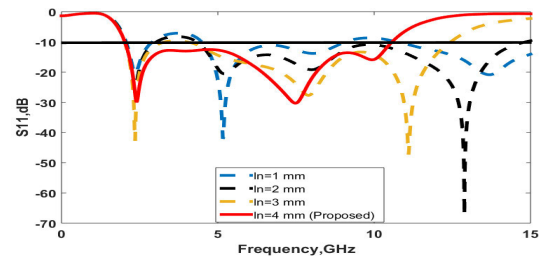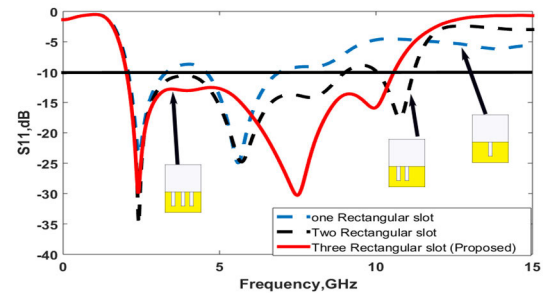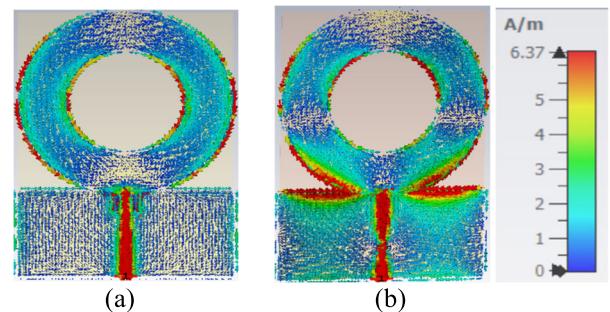
efficiency, and the 2D and 3D far-field radiation patterns. Figure 12 visually illustrates the detailed surface current distribution at frequencies of 2.4 GHz and 7.48 GHz. In the prototype, the predominant concentration of surface current is evident along the lower edges of the slotted circular disc radiating patch, encircling the feeding line, and in close proximity to both the circular slot and the rectangular-shaped slots on the lower ground. Notably, the distribution of current within these lower ground slots plays a pivotal role in achieving resonance within the specified operating frequency band. Figure 13 presents the three-dimensional radiation pattern of the proposed antenna at both 2.4 GHz and 7.48 GHz. This representation provides valuable insights into the antenna's radiation characteristics and directional performance at these specific frequencies.

The analysis reveals that the antenna predominantly emits radiation in the (-) Z direction, maintaining consistently
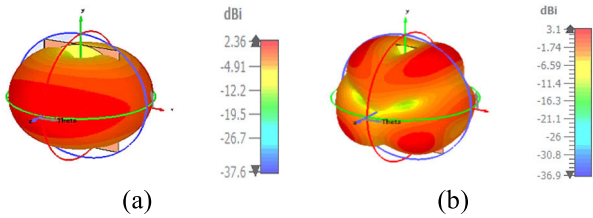
FIGURE 13. Simulated 3D far field radiation pattern: (a) at 2.4 GHz (b) at 7.48 GHz.
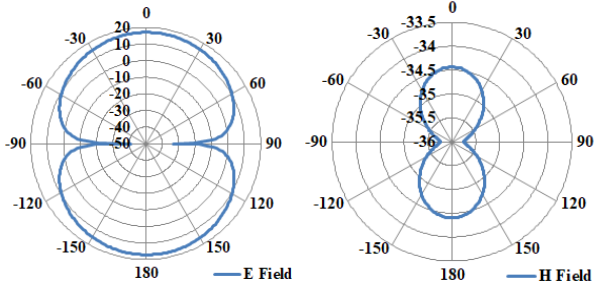

FIGURE 15. Simulated 2D far-field radiation patterns toward the (-) Z direction at 7.48 GHz: (a) E – Field (b) H - Field.

FIGURE 14. Simulated 2D far-field radiation patterns toward the (-) Z direction at 2.4 GHz: (a) E – Field (b) H - Field.

FIGURE 16. Simulated maximum gain of the proposed antenna.

FIGURE 17. Radiation efficiency of the proposed antenna.

oriented lobes towards the boresight throughout the entire operating band. The prototype exhibits quasi-symmetrical near-field and far-field radiations. However, a distinct disparity in current density is observed between lower and higher frequencies. Despite uniform power excitation, lower frequencies, such as 2.4 GHz, demonstrate lower current density, resulting in nearly omnidirectional radiation patterns and diminished gain. Conversely, higher frequencies, notably 7.48 GHz, exhibit increased current density, contributing to resonance at 2.4 GHz due to slotting effects and proper current distribution. Furthermore, at higher frequencies, the prototype demonstrates nearly directive cross-polarization, influenced by fluctuating current distribution and the presence of specific slots. Figures 14 and 15 depict the normalized simulated 2D E-plane ($\phi = 0$) and H-plane ($\phi = 90$) far-field radiation patterns of the antenna at 2.4 GHz and 7.48 GHz, respectively. Remarkably, the H-plane radiation patterns display expanding beam-widths towards the boresight direction compared to the E-plane patterns. Additionally, Figure 16 outlines the simulated gain of the antenna across different frequencies. The proposed antenna achieves substantial gain while maintaining a compact design compared to other antennas reported for head disease detection. Elevated gain is particularly advantageous for applications related to head disease detection. The proposed prototype, boasting a gain of 2.36 dBi at 2.4 GHz and 3.1 dBi at 7.48 GHz, is well-suited for head diagnosis applications due to its enhanced gain. Figure 17 illustrates the simulated radiation efficiency of the prototype across various frequencies. The analysis indicates that the average radiation efficiency of the proposed prototype is approximately 90.4%, peaking at 110% across the entire operating bandwidth due to the antenna's higher
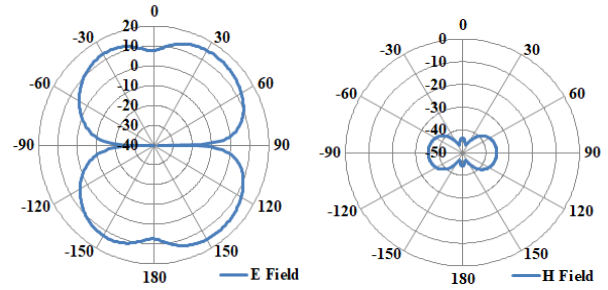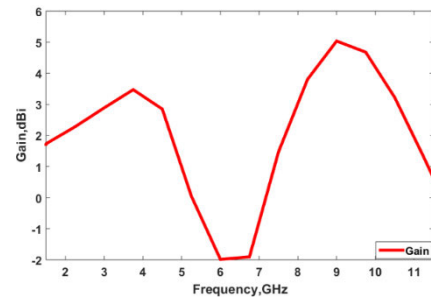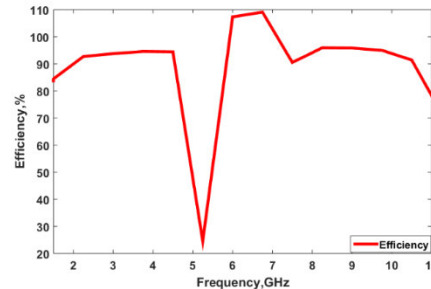
gain. Ultimately, the incorporation of various modification structures, including trapezoidal parasitic components, a rectangular ground plane, and a slotted circular-shaped patch, mitigates additional excitations, resulting in an improved operational frequency band. Notably, the efficiency is 92.5% at 2.4 GHz and 90.5% at 7.48 GHz.

V. UTILIZATION OF THE PROPOSED ANTENNA FOR HEAD DIAGNOSES

The human head comprises six distinctive tissue layers, encompassing skin, fat, bone (or skull), cerebral spinal fluid (CSF), gray matter, and white matter, each characterized by unique dielectric properties and electrical conductivity. It is imperative to consider the variations in these properties across individuals and age groups for a comprehensive analysis [21]. This study evaluates the antenna's efficacy by incorporating diverse dielectric properties and thicknesses of tissue layers, accounting for the inherent variability among individuals and

TABLE 2. The electrical attributes of the diverse tissues in the hemisphere head model at 2.4 GHz.

Tissue	Thickness (mm)	Relative permittivity	Conductivity (S/M)
Skin	0.5	43	0.89
Fat	1	5.44	0.05
Skull	3	12.36	0.15
CSF	0.5	68.43	2.45
Gray Matter	7	52.28	0.98
White Matter	75.25	38.57	0.62
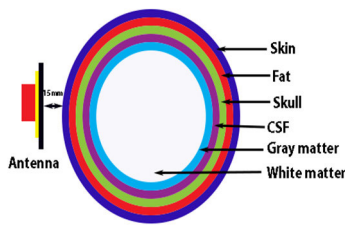
FIGURE 18. Cross-sectional perspectives of a hemisphere head model featuring tissues in six layers.

FIGURE 19. Cross-sectional perspectives of a hemisphere Hugo head model.

FIGURE 20. Antenna reflection coefficient in: (a) Free space (b) In presence of six-layer phantom.

across different age groups. Observations reveal that skin thickness and skull/bone thickness can vary from 0.5 mm to 1.5 mm and 3 mm to 10 mm, respectively, particularly in individuals over the age of 5. Utilizing the three-dimensional (3D) CST 2019 software, the simulation incorporates three different thicknesses for the skin and bone layers, representing a range pertinent to the proposed antenna's application. The simulation setup includes a basic cross-section of the hemisphere model, providing a representative structure of the human head (Figure 18-19). The electrical characteristics and respective thicknesses of various tissues in the hemisphere head model are meticulously outlined in Table 2.

In the simulation environment, the antenna is strategically positioned 15 mm away from the skin layer of the hemisphere head model, featuring six tissue layers and a radius of 100 mm. This 15 mm distance is carefully selected as the minimum between the skin layer and the antenna, ensuring minimal reflection loss below −10 dB.

Fig. 20 visually depicts the reflection coefficient of the proposed antenna under three conditions: in a free space environment, when surrounded by a six-layer phantom, and when positioned near a Hugo head. The outcomes reveal a significant resemblance between the responses observed with the six-layer phantom and the Hugo head. This suggests that, when assessing antenna sensitivity in scenarios involving brain conditions and alterations in dielectric properties, the six-layer phantom serves as a dependable alternative to the more intricate Hugo head setup. This substitution is endorsed due to its capability to yield precise and accurate results without the complexity associated with using the Hugo head. An analysis of Figure 21 and figure 22 demonstrates that microwave signals possess a notable ability to
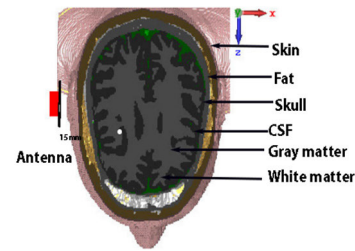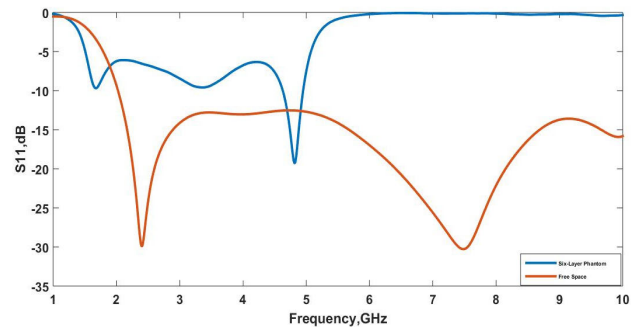
penetrate roughly two-thirds of the internal space within the human head, attributed to the inherent directional characteristics of radiation. This observation underscores the potential applications of the proposed antenna prototype, particularly in the realm of head diagnostics. The envisioned antenna shows promise for early detection in various head-related conditions, including malignant tissue, brain atrophy, lateral ventricle enlargement, and alterations in the dielectric properties of brain tissues. The antenna's capability to interact with and penetrate these specific aspects of the human head positions it as a valuable and non-invasive tool for advancing diagnostic capabilities in the field of neurological health. The detailed exploration of microwave signal penetration emphasizes the antenna's potential significance in contributing to early and accurate diagnosis of diverse neurological conditions. Figures 21 and 22 demonstrate how the antenna field penetrates in the xz-plane for both H-field and h-field using the Hugo head model at frequencies of 2.4 GHz and 7.48 GHz

VI. MODELING ALZHEIMER'S DISEASE USING A SIX-LAYER BRAIN TISSUE PHANTOM

Alzheimer's disease, a progressive neurodegenerative disorder [22], carries significant implications for the brain, affecting aspects such as brain atrophy, lateral ventricle enlargement, and alterations in the dielectric properties of gray and white matter. This condition is characterized by widespread neuronal loss and damage to brain cells [23], resulting in an overall reduction in brain volume, commonly referred to as brain atrophy. Regions critical for memory and
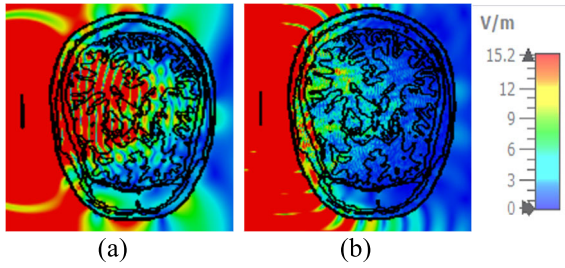
FIGURE 21. Distribution of antenna field penetration in the xz-plane for the H-field with the Hugo head model at: (a) 2.4 GHZ (b) 7.48 GHz.
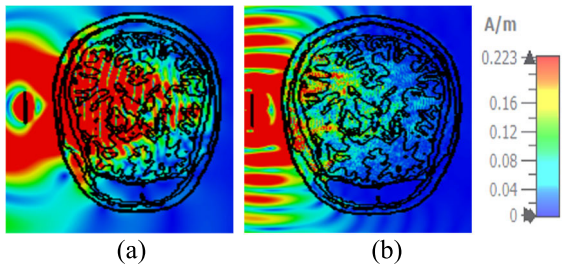

FIGURE 22. Distribution of antenna field penetration in the xz-plane for the E-field with the Hugo head model at: (a) 2.4 GHZ (b) 7.48 GHz.

TABLE 3. Brain atrophy stages.

Brain atrophy (%)	Gray matter thickness (mm) reduction	White matter thickness (mm) reduction	CSF thickness (mm) expansion
Stage 1: 0 %	7	75.25	0.5
Stage 2: 15 %	5.95	63.96	12.84
Stage 3: 20 %	5.6	60.2	16.95
Stage 4: 25 %	5.25	56.43	21.07

cognition, including the hippocampus and cerebral cortex, are particularly susceptible to atrophy, contributing to the observed cognitive decline in individuals with Alzheimer's. The gradual loss of brain tissue leads to the shrinking of these pivotal regions.

Lateral ventricles, fluid-filled cavities within the brain involved in cerebrospinal fluid circulation [24], undergo enlargement in Alzheimer's disease due to the atrophy and loss of brain tissue. As brain tissue diminishes, the ventricles may expand, resulting in a noticeable increase in size. This ventricular enlargement is a recurring feature observed in neuroimaging studies of individuals with Alzheimer's and signifies structural changes within the brain.

The dielectric properties of brain tissues, encompassing gray and white matter, are influenced by their composition and structural integrity. In Alzheimer's disease, the accumulation of abnormal protein aggregates, such as beta-amyloid plaques and tau tangles, can modify the dielectric properties of affected brain regions. Changes in the electrical properties of tissues are observable, and these alterations may be detectable through methods such as electromagnetic imaging or other techniques relying on dielectric contrast. Understanding the impact of Alzheimer's disease on brain structure and properties is crucial for both diagnosis and potential therapeutic interventions [26]. Research in this field aims to unravel the intricate details of these changes, leading to improved methods for early detection and targeted treatments for individuals affected by Alzheimer's disease.

Alzheimer's disease unfolds in three primary stages: early (mild), middle (moderate), and late (severe) [27]. The early stage is characterized by mild memory loss and subtle cognitive challenges. The middle stage involves a noticeable decline in cognitive function, impacting daily tasks and behavior. The late stage represents the most advanced phase, marked by profound cognitive decline, dependence on others for care, and severe behavioral changes. While these stages, outlined in Table 6, provide a general framework, the progression varies among individuals, emphasizing the need for personalized care and ongoing research in understanding and managing Alzheimer's disease. Early diagnosis and meticulous care planning remain crucial throughout the disease's progression. Subsequently, attention is focused on modeling brain atrophy, lateral ventricle enlargement, and changes in dielectric properties, with the development of a six-layer phantom to represent each stage of Alzheimer's disease.

A. MODELING THE BRAIN ATROPHY

In the initial phase of simulating brain atrophy [12], a systematic approach was employed to systematically decrease the thickness of both gray and white matter layers. The removed tissue was substituted with a cerebrospinal fluid (CSF) layer, resulting in the establishment of a six-layer tissue phantom. The first trial entailed a 5% uniform thickness reduction, followed by a subsequent trial introducing an additional 5% reduction along with a thicker CSF layer, leading to a cumulative 10% reduction from the original model. Subsequent trials incorporated models with more significant size reductions (20% and 25%) in both gray and white matter layers, as delineated in Table 3. These modifications were implemented to faithfully replicate varying degrees of brain atrophy for research purposes, as depicted in Figure 24.

B. MODELING THE ENLARGEMENT OF LATERAL VENTRICLES

Various sizes of synthetic phantoms were meticulously designed to create cerebrospinal fluid (CSF) objects with heightened dielectric properties. These CSF objects were subsequently introduced into the six-layer phantom, as outlined in Table 6. As depicted in Figure 21, it is essential to note that the CSF object shares identical dielectric properties with the CSF layer [12].

TABLE 4. Lateral ventricle enlargement stages.

lateral ventricle enlargement	White thickness (mm) reduction	CSF object Radius (mm) augmentation
Stage 1	75.25	0
Stage 2	63.96	11.5
Stage 3	60.2	15.5
Stage 4	56.43	18.5

TABLE 5. Dielectric values of brain tissues of AD brain at 2.4 GHz.

Stage	$(\varepsilon r, \sigma)$ for gray matter	$(\varepsilon r, \sigma)$ for white matter	$(\varepsilon r, \sigma)$ for CSF
Stage 1	52.28 and 0.98	38.57 and 0.62	68.43 and 2.45
Stage 2-4	41.36 (20.87% decrease) And 1.138 (16.17% increase)	32.71 (15.17% decrease) And 0.892 (44.88% increase)	58.16-34.215(15%-50% decrease) and 2.81- 3.67 (15%-50% increase)

C. MODELING THE CHANGES IN DIELECTRIC PROPERTIES OF GRAY AND WHITE MATTER

At the frequency of 2.4 GHz, as depicted in Table 5, the gray matter within the Alzheimer's disease (AD)-affected brain demonstrates a 20.87% reduction in relative permittivity compared to the healthy brain, accompanied by a 16.17% increase in the imaginary component. Similarly, the white matter in the AD-affected brain exhibits a 15.17% decrease in relative permittivity and a 44.88% rise in the imaginary part at the same frequency relative to the healthy brain. These findings indicate distinct alterations in electromagnetic properties for both gray and white matter associated with Alzheimer's disease [13].

A study investigating the impact of Alzheimer's disease (AD) proteins on dynamic parameters (DPs) and cerebrospinal fluid (CSF) revealed noteworthy changes. Specifically, the analysis disclosed a decrease in relative permittivity and an increase in the loss tangent when compared to normal CSF samples [14]. Detailed information regarding the dielectric properties of cerebrospinal fluid (CSF) in Alzheimer's disease (AD) is currently lacking. Consequently, for each stage, a range of variations in the relative permittivity and conductivity of CSF and brain in AD can be established, as outlined in Table 5, attributed to the accumulation of beta and tau proteins.

D. MODELING THE AD BRAIN IN VARIOUS THREE STAGES

Advancing with the incorporation of three Alzheimer's disease biomarkers, the modeling of an AD-infected brain is refined to accurately depict the distinctive features of the three stages of AD. The parameters encompassed in this modeling encompass the thickness of the cerebrospinal
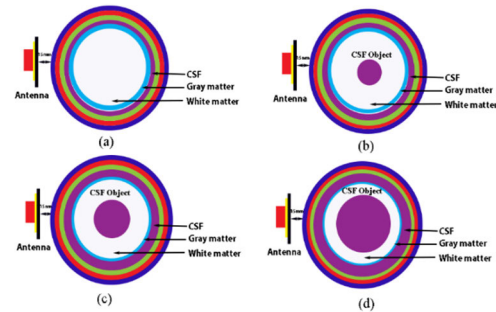

FIGURE 23. Cross-sectional perspectives of a hemisphere head model featuring various phases of an Alzheimer's disease-affected brain: (a) Healthy (b)Mild AD (c) Moderate AD and (d) Serve AD.

fluid (CSF) layer, gray matter thickness, and white matter thickness, aligning with the manifestation of brain atrophy. Furthermore, variables such as the volume of the CSF object contribute to illustrating lateral ventricle enlargement. Additionally, the relative permittivity and conductivity of gray and white matter serve as indicators of dielectric changes associated with AD. These pivotal parameters are succinctly outlined in Table 6.

Following the comprehensive modeling, the simulation extends to assessing S11 for each stage, encompassing the healthy stage as well. This simulation, as illustrated in Figure 21, stands as a critical analysis to evaluate the antenna's sensitivity in effectively detecting and differentiating each distinct stage of Alzheimer's disease.

VII. SENSITIVITY OF THE ANTENNA IN DETECTING ALZHEIMER'S DISEASE IN THE BRAIN

In this section, we thoroughly examine critical aspects to validate the antenna's performance, covering effectiveness analysis, an investigation into microwave signal penetration depth through head tissues for comprehensive data collection, sensitivity analysis, and a specific absorption rate (SAR) analysis tailored for a human head model suitable for practical applications. The proposed antenna, designed for diagnosing head conditions using microwave technology, presents several merits: (i) it demonstrates improved reflection coefficients concerning variations in skin and bone layers' thickness, as well as changes in the dielectric properties of head tissues like gray matter, white matter, and cerebrospinal fluid (CSF), (ii) it exhibits enhanced reflection coefficients during scanning of both healthy and unhealthy heads, including different stages of Alzheimer's disease, (iii) it upholds relatively low SAR levels and favorable near-field directivity, thereby minimizing the potential for tissue damage compared to reported SAR levels, (iv) assessing the current density near the human head is pivotal to ensuring the effectiveness and safety of antenna systems in close proximity to living tissues.

A. SINGLE ANTENNA

Figure 22 demonstrates alterations in the reflection coefficient resulting from brain atrophy, ventricle enlargement,

TABLE 6. AD brain stages.

AD stage	Gray matter thickness (mm)	White matter thickness (mm)	CSF thickness (mm)	CSF ($\varepsilon r, \sigma$)
	CSF object Radius (mm)	Gray matter ($\varepsilon r, \sigma$)	White matter ($\varepsilon r, \sigma$)	
Stage 1:	7	75.25	0.5	68.43 and 2.45
Healthy	0	52.28, 0.98	38.57, 0.62	
Stage 2:	5.95	63.96	12.84	58.16 and 2.81
Mild	11.5	41.36,1.138	32.71, 0.892	
Stage 3:	5.6	60.2	16.95	51.32 and 3.06
Moderate	15.5	41.36,1.138	32.71, 0.892	
Stage 4:	5.25	56.43	21.07	34.21 and
Serve	17.5	41.36,1.138	32.71, 0.892	3.67

and changes in dielectric properties within the healthy brain model. In Figure 24(a), the difference in reflection coefficient between the healthy brain and mild Alzheimer's disease (AD) is apparent, revealing a frequency shift from 1.66 to 1.823 GHz, 4.8 to 6.186 GHz, and the emergence of a new resonance frequency at 8.64 GHz. In Figure 24(b), the disparity in reflection coefficient between the healthy brain and Moderate Alzheimer's disease (AD) is observable, indicating a frequency shift from 1.66 to 1.848 GHz, 4.8 to 6.063 GHz, and the emergence of a new resonance frequency at 7.85 GHz. In Figure 24(c), the reflection coefficient difference between a healthy brain and severe Alzheimer's disease (AD) is noticeable. The frequency shift is observed at 4.8 to 4.48 GHz, with no shift detected at 1.66 GHz, and there is no appearance of a new resonance frequency. Figure 24(d) illustrates the contrast in reflection coefficient between each stage and a healthy brain.

The calculation of current density is pivotal when the antenna is positioned near the human head, offering crucial insights into electromagnetic field exposure. Understanding these density variations aids in assessing potential health implications and optimizing antenna design for both effectiveness and safety in practical applications. Figure 25 depicts the antenna's current density adjacent to a healthy brain phantom in contrast to various stages of Alzheimer's disease (mild, moderate, and severe). It is noteworthy that the corresponding values are 102, 230, 274, and 209 A/m^2 for the respective stages. Emphasizing the significance of current density near the head, this analysis provides insights into the variations associated with different Alzheimer's stages.

The Specific Absorption Rate (SAR) is a crucial consideration in microwave head imaging applications to ensure safety during exposure to the human body. Since the proposed antenna is designed for head imaging, this research thoroughly investigates safety concerns. The examination adheres to the IEEE public radiation exposure limit of 1.6 W/kg for 10 grams [26]. The SAR distribution within the six-layer tissues for healthy head model and serve AD model is depicted in Figure 26, revealing that maximum SAR values are predominantly located just outside the head tissue layers. Notably, the calculated maximum SAR is 0.734 W/kg at 2.4 GHz and 0.00238 W/kg at 7.48 GHz for healthy brain and 1.47 W/kg at 2.4 GHz and 0.00605 W/kg at 7.48 GHz for serve AD brain, both of which fall below the standard limit of 1.6 W/kg, ensuring compliance with safety regulations.

B. ARRAY OF ANTENNAS

Utilizing an array of antennas around the human head in Alzheimer's disease diagnosis is crucial due to its capacity for heightened sensitivity and broader spatial coverage. This array allows for more thorough data collection, detecting subtle electromagnetic variations associated with different disease stages. Improved sensitivity and localization capabilities contribute to a more accurate and detailed assessment, potentially enabling early detection and intervention in Alzheimer's disease diagnosis. The configuration of the antenna array scanning setup is depicted in Figure 27 (a-b). In this arrangement, four antenna elements are situated 15 mm from the skin layer, with a 15 mm gap between each element, encircling the six-layers head tissues.

Figure 28 illustrates the S-parameters (S1,1 to S4,1) response when antenna 1 is activated for the healthy head setup (without Alzheimer's disease) and the unhealthy head setup (with Alzheimer's disease), with the other three antennas receiving scattered signals. While the reflection response of the transmitting antenna remains relatively stable in the complete scanning arrangement compared to the single-antenna simulation predictions, there is noticeable distortion in the backscattering signal across the three graphs in Figure 28(a-d).

Fig. 29 presents a detailed analysis of the S2,1, S3,1, and S4,1 parameter, comparing a healthy brain to three distinct stages of Alzheimer's disease. In Figure 29(a), the nuanced differences among the four scenarios manifest prominently within the 5 GHz band. This band delineates resonance frequencies for each case, illustrating a comprehensive range
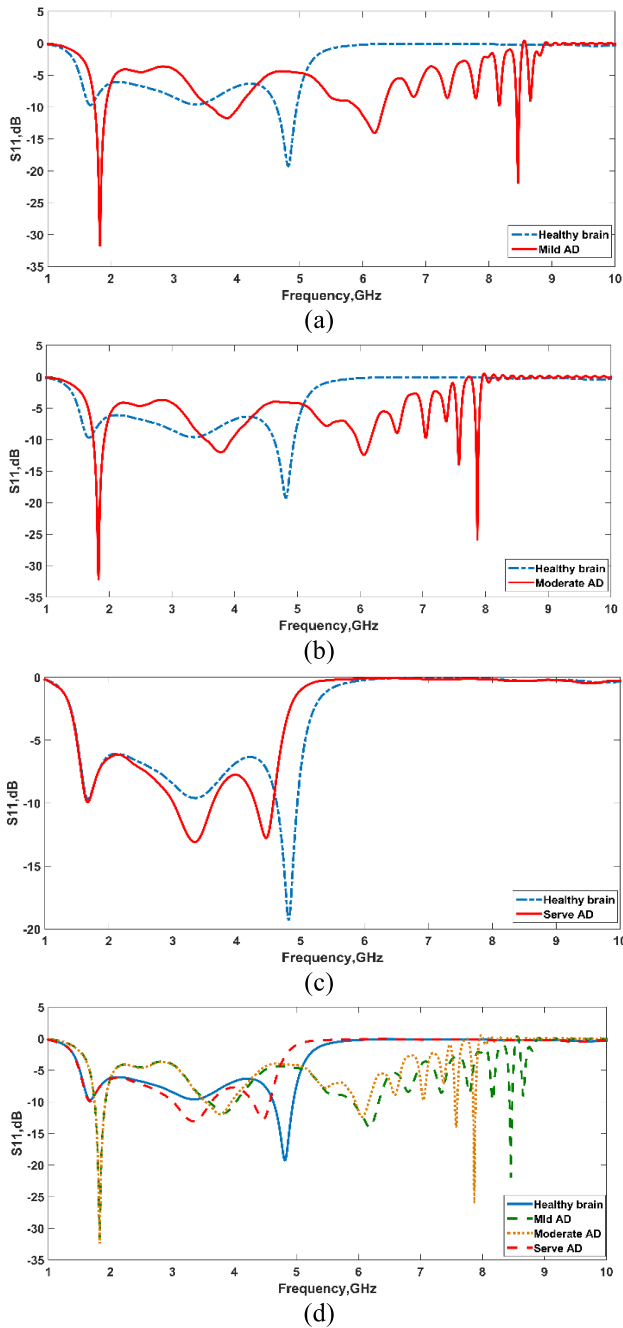
(a)

(b)

(c)

FIGURE 24. Reflection coefficients observed in different AD stages versus healthy brain: (a) Mild AD (b) Moderate AD (c) Serve AD (d) three stages.

FIGURE 25. Current density observed in different AD stages versus healthy brain at 2.4 GHz: (a) Healthy brain (b) Mild AD (c) Moderate AD (d) Serve AD.

FIGURE 26. SAR and its internal distribution within the six-layer tissues phantom of head model. Maximum SAR values were determined at different frequencies in the healthy brain and Serve AD at: (a) healthy brain at 2.4 GHz (b) healthy brain at 7.48 GHz (c) Serve AD at 2.4 GHz (d) Serve AD at 7.48 GHz.

extending up to 10 GHz for S2,1. The intricate variations persist in Figure 29(b) and Figure 29(c), where the 5 GHz band reveals distinctive resonance frequencies for each case, reaching up to 10 GHz for S3,1 and S4,1, respectively. This thorough examination provides a comprehensive understanding of the resonance frequency dynamics across the frequency spectrum, offering insights into the specific characteristics of different Alzheimer's disease stages compared to a healthy brain. The notable distinctions among the four stages become more apparent when employing a configuration of four array
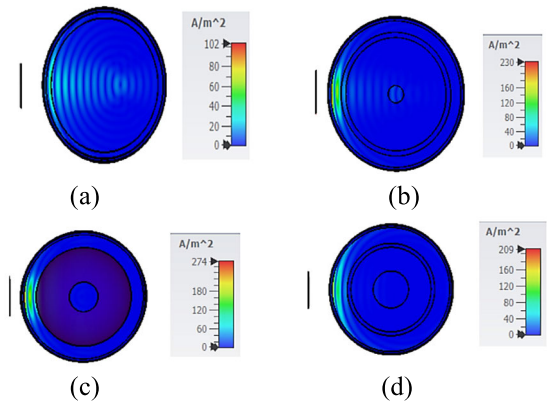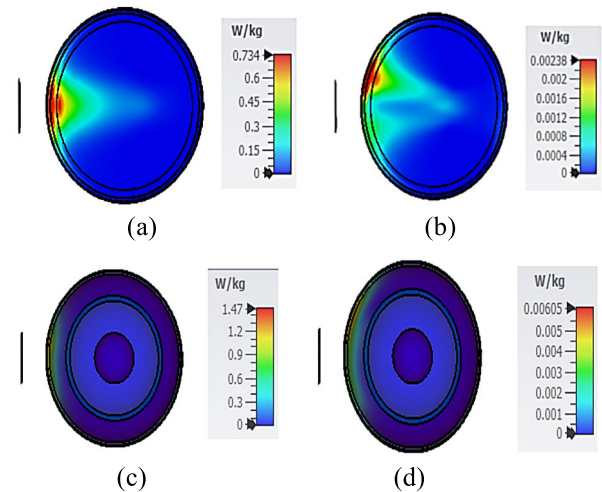
antennas positioned around a human phantom, as compared to the use of a single antenna. In this multi-antenna setup, the nuanced variations in signals and responses across the different Alzheimer's disease stages are more finely detected and characterized. The increased sensitivity of the array configuration enhances the resolution and accuracy of the observations, providing a detailed and comprehensive understanding of the electromagnetic interactions associated with each stage.

Figure 30 intricately presents the Specific Absorption Rate (SAR) distribution within the head model, offering a nuanced view of how SAR values are distributed across different layers of the head tissue. Noteworthy in the visual representation is the discernible concentration of the highest SAR values on the outer layers of the head tissue. Of particular importance is the consistent adherence of the computed maximum SAR values, specifically at the operating frequency of 2.4 GHz
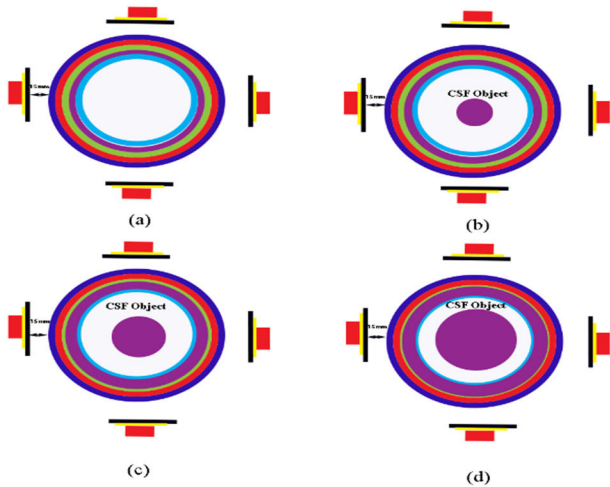
FIGURE 27. Proposed antenna arrays simulation with head model featuring various phases of an Alzheimer's disease-affected brain: (a) Healthy (b)Mild AD (c) Moderate AD and (d) Serve AD.

for antennas 1, 2, 3, and 4, to the rigorous safety standards outlined by the IEEE. These values consistently remain well below the established public radiation exposure limit of 1.6 W/kg for a 10 g mass, as stipulated by the IEEE guidelines. This robust adherence to safety standards is visually corroborated in both scenarios presented in Figure 28— Figure 30(a) portraying a scenario with a healthy brain and Figure 30(b) depicting a brain affected by Alzheimer's disease. The careful examination of SAR distribution not only underscores the antenna's commitment to safety but also assures that potential health risks associated with radiation exposure are effectively mitigated within the specified limits brain.

A specific focus has been directed towards achieving high temporal resolution in functional neuroimaging. These methodologies exploit variations in dielectric permittivity and electrical conductivity between healthy and diseased body regions, employing antenna arrays for signal transmission and reception, thereby facilitating precise diagnosis and disease analysis. The integration of Ultra-wideband (UWB) technology further enhances the resolution and accuracy of microwave imaging systems.

Current research efforts in the field are singularly focused on pushing the boundaries of Alzheimer's disease detection, employing microwave sensors as elucidated in Table 7. This sustained investigation highlights a perpetual exploration of the capabilities inherent in microwave technology for medical diagnostics. It accentuates the persistent endeavors to fine-tune and enhance detection methods, with a specific emphasis on the intricate landscape of Alzheimer's disease. Notably, in contrast to earlier research, there is a notable absence of a simulated model, and the absence of mention of specific absorption rate (SAR) values in prior studies is also evident. These current endeavors mark a distinct departure, placing a premium on refining and optimizing
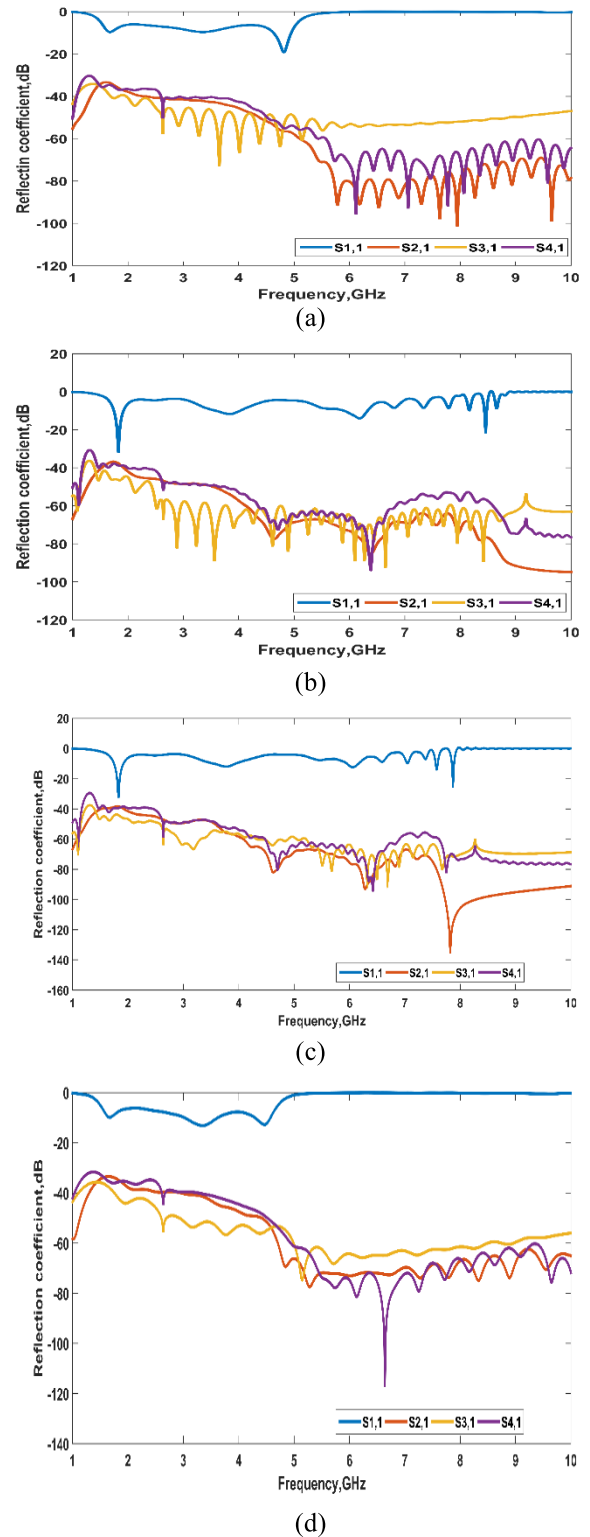

FIGURE 28. Reflection coefficients observed for 4 antenna array in different AD stages versus healthy brain: (a) Mild AD (b) Moderate AD (c) Serve AD (d) 3 stages.

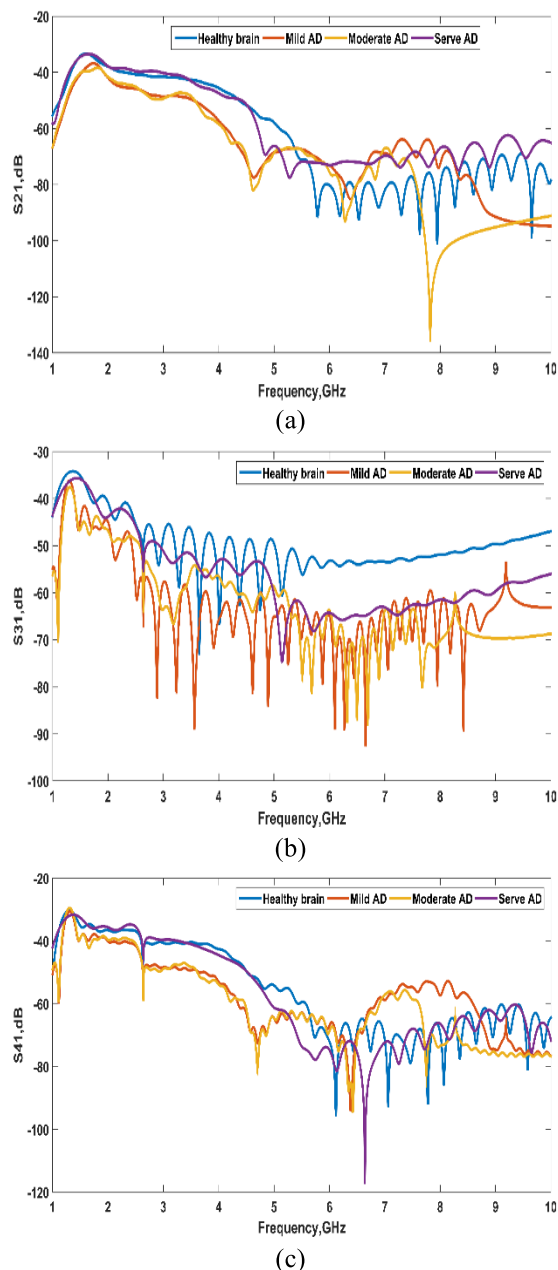microwave-based diagnostic techniques, particularly in the nuanced context of Alzheimer's disease, where simulated

(a)

(b)

(c)

FIGURE 29. Reflection coefficients in diverse stages of Alzheimer's disease versus a healthy brain: (a) S2,1 (b) S3,1 (c) S4,1.

(a)

(b)

FIGURE 30. SAR distribution inside six-layer head tissues model when antenna −1, antenna −2, antenna-3 and antenna-4 are in operating at 2.4 GHz: (a) Healthy brain (b) AD brain.

models and SAR values play a crucial role. Moreover, it's worth noting that the existing body of research lacks attention to the crucial aspect of dielectric changes within gray and white matter. In the current landscape, there is a distinct absence of concern or investigation regarding alterations in dielectric properties specific to these brain tissues. This observation underscores a significant gap in previous studies, indicating a need for dedicated exploration and understanding of how microwave technology interacts with the distinct dielectric characteristics of gray and white matter. The absence of this concern in prior research underscores
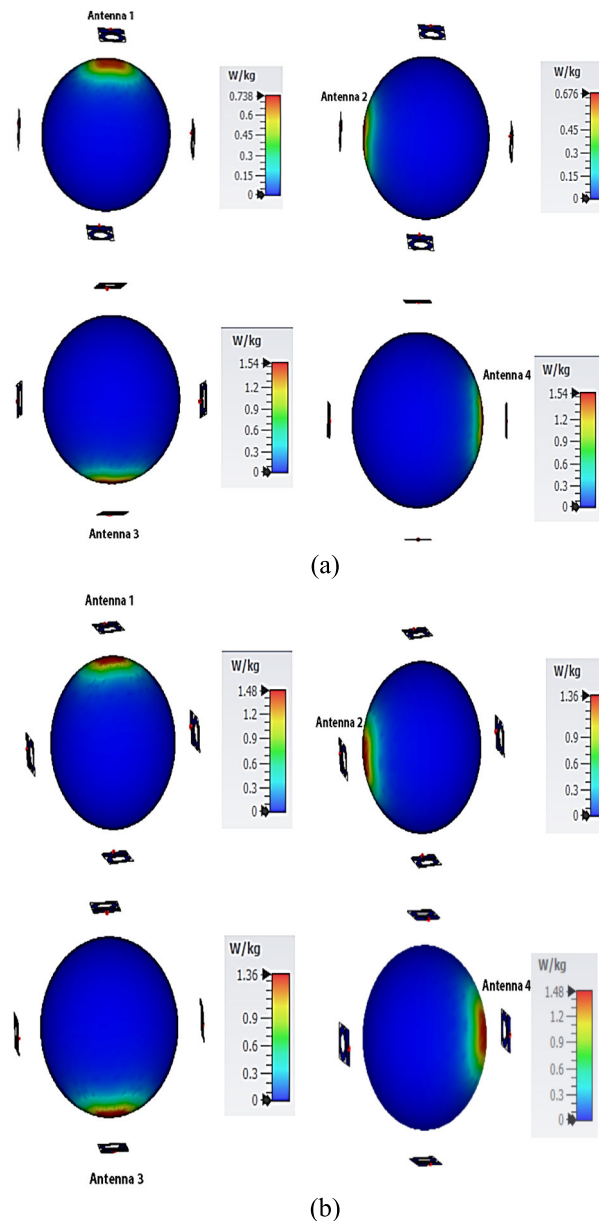
the novelty and importance of addressing this specific aspect in the ongoing endeavors to enhance Alzheimer's disease detection. Additionally, a notable deficiency in prior research is the absence of a simulated brain model that incorporates all Alzheimer's disease biomarkers collectively. The existing studies have not encompassed a comprehensive simulation that considers the simultaneous presence and interaction of various biomarkers associated with Alzheimer's disease. This critical gap underscores the need for a more holistic and integrated approach in the simulation of brain models to better understand the intricate interplay of multiple biomarkers. The absence of such a comprehensive simulated model in earlier

TABLE 7. Contrast with comparable research.

Ref.	Health sector	Microwave technology	Operating frequency (GHz) and gain (dBi)	SAR (W/Kg)	Core insights
[12]	Alzheimer's disease	A hat with six symmetrical monopole bidirectional antenna elements is designed for wearables.	0.8 to 3 GHz band - gain not mentioned	0.0115-0.135 W/Kg	Through simulation and experimental validation, the hat is specifically crafted to detect brain atrophy. Real lamb brain tests within a human head phantom are employed for thorough testing and verification.
[13]	Alzheimer's disease	Six carefully crafted ultra-wideband antennas encircle the head phantom.	200 MHz to 3 GHz- gain not mentioned	not mentioned	Dielectric measurements were collected from the grey and white matter regions of brain tissues with pronounced pathology from Alzheimer's disease, covering frequencies ranging from 200 MHz to 3 GHz.
[14]	Alzheimer's disease	implantable antenna consists of a semi-circular patch connected to two meandered transmission lines	0.25 – 0.7 GHz - gain not mentioned	not mentioned	The study establishes a robust link between canine and human CSF, confirming the suitability of canines for AD-related research. In CSF affected by AD, there is a noticeable decrease in relative permittivity and an increase in the loss tangent compared to normal CSF.
This work	Alzheimer's disease	Four ultra- thin wearable antennas	2.02–10.57 GHz and 2.36 - 3.1 dBi respectively	0.734 - 0.00238 W/Kg	This research categorizes three phases of Alzheimer's disease, where the phantoms for each stage simulate brain atrophy, ventricle enlargement, and changes in dielectric properties for gray matter, white matter, and cerebrospinal fluid (CSF).

research highlights a distinct opportunity and necessity for current investigations to advance towards a more encompassing understanding of Alzheimer's disease pathology.

VIII. CONCLUSION

This research offers a groundbreaking contribution to the field by introducing a novel algorithm for simulating an Alzheimer's disease (AD) brain model and developing a patch antenna with ultra-wideband capabilities for non-invasive AD detection. The algorithm addresses a critical gap, providing a cost-effective and safer alternative to traditional diagnostic techniques. The patch antenna demonstrates remarkable performance, showcasing potential for effective AD tracking. Practical advantages include non-invasiveness, cost-effectiveness, and promising diagnostic capabilities. However, limitations exist, requiring further validation through clinical trials and exploration of applicability to other neurodegenerative diseases. Future research suggestions emphasize collaboration with medical professionals, refining the algorithm for individual variations, and optimizing the antenna for scalability. Overall, this research marks a significant advancement in neurodegenerative disease diagnostics with potential for practical implementation and future developments.

REFERENCES

[1] L. C. Walker and H. LeVine, "The cerebral proteopathies," *Neurobiol Aging*, vol. 21, no. 4, pp. 559–561, 2000.

[2] C. A. Taylor, S. F. Greenlund, L. C. McGuire, H. Lu, and J. B. Croft, "Deaths from Alzheimer's disease—United States, 1999–2014," *MMWR Morb Mortal Wkly Rep.*, vol. 66, pp. 521–526, Jan. 2017.

[3] A. Association, "2019 Alzheimer's disease facts and figures," *Alzheimer's Dementia*, vol. 15, no. 3, pp. 321–387, Mar. 2019.

[4] Alzheimer's Soc., *What is Alzheimer's disease: Factsheet 401LP July 2014*, Factsheet 401LP, U.K., 2014, pp. 1–10.

[5] *England and Wales; Mortality Statistics: Deaths Registered in England and Wales (Series DR). Scotland: National Records of Scotland Vital Events Reference Tables. Northern Ireland; Northern Ireland Statistic & Research Agency Registrar General Annual Report*, Office Nat. Statist., U.K., 2017.

[6] C. Reitz and R. Mayeux, "Alzheimer disease: Epidemiology, diagnostic criteria, risk factors and biomarkers," *Biochem. Pharmacol.*, vol. 88, no. 4, pp. 640–651, Apr. 2014.

[7] C. R. Harrington, "The molecular pathology of Alzheimer's disease," *Neuroimaging Clinics*, vol. 22, no. 1, pp. 11–22, 2012.

[8] C. Z. W. Hassell, J. S. Thompson, B. Mulgrew, and P. M. Grant, "A comparison of detection algorithms including BLAST for wireless communication using multiple antennas," in *Proc. 11th IEEE Int. Symp. Pers. Indoor Mobile Radio Commun.*, Sep. 2000, pp. 698–703.

[9] K. Aliqab, I. Nadeem, and S. R. Khan, "A comprehensive review of in-body biomedical antennas: Design, challenges and applications," *Micromachines*, vol. 14, no. 7, p. 1472, 2023.

[10] E. Razzicchia, I. Sotiriou, H. Cano-Garcia, E. Kallos, G. Palikaras, and P. Kosmas, "Feasibility study of enhancing microwave brain imaging using metamaterials," *Sensors*, vol. 19, no. 24, p. 5472, Dec. 2019.

[11] E. C. Ngai, "Compact and low-cost microwave helmet brain scanner for monitoring Parkinson's disease," in *Proc. IEEE Int. Symp. Antennas Propag. USNC/URSI Nat. Radio Sci. Meeting*, Jul. 2018, pp. 1141–1142.

[12] I. M. Saied and T. Arslan, "Noninvasive wearable RF device towards monitoring brain atrophy and lateral ventricle enlargement," *IEEE J. Electromagn., RF Microw. Med. Biol.*, vol. 4, no. 1, pp. 61–68, Mar. 2020, doi: 10.1109/JERM.2019.2926163.

[13] I. Saied, T. Arslan, S. Chandran, C. Smith, T. Spires-Jones, and S. Pal, "Non-invasive RF technique for detecting different stages of Alzheimer's disease and imaging beta-amyloid plaques and tau tangles in the brain," *IEEE Trans. Med. Imag.*, vol. 39, no. 12, pp. 4060–4070, Dec. 2020, doi: 10.1109/TMI.2020.3011359.

[14] M. Manoufali, A. T. Mobashsher, B. Mohammed, K. Bialkowski, P. C. Mills, and A. Abbosh, "Implantable sensor for detecting changes in the loss tangent of cerebrospinal fluid," *IEEE Trans. Biomed. Circuits Syst.*, vol. 14, no. 3, pp. 452–462, Jun. 2020.

[15] I. M. Saied, S. Chandran, and T. Arslan, "Integrated flexible hybrid silicone-textile dual-resonant sensors and switching circuit for wearable neurodegeneration monitoring systems," *IEEE Trans. Biomed. Circuits Syst.*, vol. 13, no. 6, pp. 1304–1312, Dec. 2019.

[16] (2008). *ULTRALAM 3000 Liquid Crystalline Polymer Circuit Material*. Accessed: Nov. 6, 2020. [Online]. Available: http://www.clarke.com.au/pdf/ULTRALAM__3000_LCP_laminate_data_sheet__ULTRALAM_3850.pdf

[17] S. A. R. Parizi, "Bandwidth enhancement techniques," in *Trends in Research on Microstrip Antennas*, S. Chattopadhyay, Ed. Rijeka, Croatia: InTech, 2017, pp. 3–37.

[18] M. Huynh, "Wideband compact antennas for wireless communication applications," Ph.D. dissertation, Dept. Electr. Comput. Eng., Virginia Polytech. Inst. State Univ., Blacksburg, VA, USA, 2004.

[19] X. Chen and P. J. Massey, "Operating principles and features of UWB monopoles and dipoles," in *Proc. IET Seminar Ultra Wideband Syst., Technol. Appl.*, Apr. 2006, pp. 131–152.

[20] M. Rokunuzzaman, A. Ahmed, T. C. Baum, and W. S. T. Rowe, "Compact 3-D antenna for medical diagnosis of the human head," *IEEE Trans. Antennas Propag.*, vol. 67, no. 8, pp. 5093–5103, Aug. 2019.

[21] R. B. Maccioni, J. P. Muñoz, and L. Barbeito, "The molecular bases of Alzheimer's disease and other neurodegenerative disorders," *Arch. Med. Res.*, vol. 32, no. 5, pp. 367–381, Sep. 2001.

[22] J. Vickers, "The cause of neuronal degeneration in Alzheimer's disease," *Prog. Neurobiol.*, vol. 60, no. 2, pp. 139–165, Feb. 2000.

[23] R. M. Fame, C. Cortés-Campos, and H. L. Sive, "Brain ventricular system and cerebrospinal fluid development and function: Light at the end of the tube: A primer with latest insights," *BioEssays*, vol. 42, no. 3, Mar. 2020, Art. no. 1900186.

[24] M. Hashimoto, E. Rockenstein, L. Crews, and E. Masliah, "Role of protein aggregation in mitochondrial dysfunction and neurodegeneration in Alzheimer's and Parkinson's diseases," *NeuroMolecular Med.*, vol. 4, nos. 1–2, pp. 21–36, 2003.

[25] S. Khan, K. H. Barve, and M. S. Kumar, "Recent advancements in pathogenesis, diagnostics and treatment of Alzheimer's disease," *Current Neuropharmacol.*, vol. 18, no. 11, pp. 1106–1125, 2020.

[26] V. Volloch, B. R. Olsen, and S. Rits, "AD 'statin': Alzheimer's disorder is a 'fast' disease preventable by therapeutic intervention initiated even late in life and reversible at the early stages," *Ann. Integrative Mol. Med.*, vol. 2, no. 1, p. 75, 2020.

[27] *IEEE Standard for Safety Levels With Respect To Human Exposure To Radio Frequency Electromagnetic Fields, 3 KHz To 300 GHz Amendment 1: Specifies Ceiling Limits for Induced and Contact Current, Clarifies Distinctions Between Localized Exposure and Spatial Peak Power Density*, Standard C95.1-2005, 2005, pp. 1–9.

FATMA TAHER (Senior Member, IEEE) received the Ph.D. degree from the Khalifa University of Science, Technology and Research, United Arab Emirates, in 2014. She is currently the Assistant Dean of the College of Technological Innovation, Zayed University, Dubai, United Arab Emirates. She has published more than 40 articles in international journals and conferences. Her research interests include signal and image processing, pattern recognition, deep learning, machine learning, artificial intelligence, and medical image analysis, especially in detecting of the cancerous cells, kidney transplant, autism, watermarking, remote sensing, and satellite images. She served as a member of the steering, organizing, and technical program committees for many international conferences. She has received many distinguished awards, such as the Best Paper Award of the first prize in the Ph.D. Forum of the 20th IEEE International Conference on Electronics, Circuits, and Systems (ICECS), the Ph.D. Forum, in December 2013. And recently, she received the United Arab Emirates Pioneers Award as the first United Arab Emirates to create a computer-aided diagnosis system for early lung cancer detection based on the sputum color image analysis, awarded by H. H. Sheik Mohammed Bin Rashed Al Maktoum, in November 2015. In addition to that, she received the Innovation Award at the 2016 Emirati Women Awards by H. H. Sheik Ahmed Bin Saeed Al Maktoum. She was the Chairperson of Civil Aviation Authority and a Patron of Dubai Quality Group and L'oréal-UNESCO for Women in Science Middle East Fellowship, in 2017. She is the Vice Chair of the IEEE United Arab Emirates Section and the Chair of the Education Committee in British Society, United Arab Emirates. She has served on many editorial and reviewing boards for international journals and conferences.

MOATH ALATHBAH received the Ph.D. degree from Cardiff University, U.K. He is currently an Assistant Professor with King Saud University, Saudi Arabia. His research interests include the development of photoelectronic, integrated electronic active and passive discrete devices, the design, fabrication, characterization of MMIC, RF and THz components, smart antennas, microstrip antennas, microwave filters, meta-materials, 5G antennas, MIMO antennas miniaturized multiband/wideband antennas, and microwave/millimeter components using micro and nano technology.

M. ABDEL-ALEIM M. received the bachelor's degree from Ain Shams University, in 2012. Currently, he is a Teaching Assistant with Ahram Canadian University and the Arab Academy for Science, Technology & Maritime Transport (AAST), Cairo, Egypt, he has dedicated himself to sharing knowledge and fostering the development of future engineers. His diverse research interests include multiple-input multiple-output (MIMO) systems, cooperative communications, digital communications, antennas design, and biomedical applications.

MOHAMED FATHY ABO SREE was born in Egypt. He received the M.Sc. degree from the Arab Academy for Science and Technology (AASTMT), in 2013, and the Ph.D. degree in electrical engineering from Ain Shams University, Egypt, in 2019. His research interests include antenna design and MW technology. He is reviewing in IEEE Access and *PIER* on-line journal.

THAMER ALGHAMDI received the B.Sc. degree from Albaha University, Al Bahah, Saudi Arabia, in 2012, the M.Sc. degree from Northumbria Newcastle University, Newcastle, U.K., in 2016, and the Ph.D. degree from Cardiff University, Cardiff, U.K., in 2023. Then, he was a Power Distribution Engineer with Saudi Electricity Company (SEC), until 2013. He was a Lecturer Assistant, from 2016 to 2018. His main research interests include power systems, power quality, the integration of renewables, and AI applications in electrical engineering.

SARA YEHIA ABDEL FATAH was born in Cairo. She received the M.Sc. degree from the Arab Academy for Science and Technology, in 2014. She is currently pursuing the Ph.D. degree with Aswan University. She is currently working as an Assistant Lecturer with the Egyptian Chinese University, Cairo, for eight years.

• • •